Supporting Information

Designing of Efficient Bifunctional ORR/OER Pt Single Atom Catalysts Based on O-terminated MXenes by First Principles Calculations

Dongxiao Kan[a,b], Dashuai Wang[a], Yingjie Cheng[a], Ruqian Lian[a], Bo Sun[a], Kaiyun Chen[b], Wangtu Huo[b], Yizhan Wang[a], Gang Chen[a], Yingjin Wei[a]*

[a]Key Laboratory of Physics and Technology for Advanced Batteries (Ministry of Education), Jilin Engineering Laboratory of New Energy Materials and Technology, College of Physics, Jilin University, Changchun 130012, P.R. China.

[b]Northwest Institute for Non-Ferrous Metal Research

*yjwei@jlu.edu.cn; 86-431-85155126

S-1 Figures

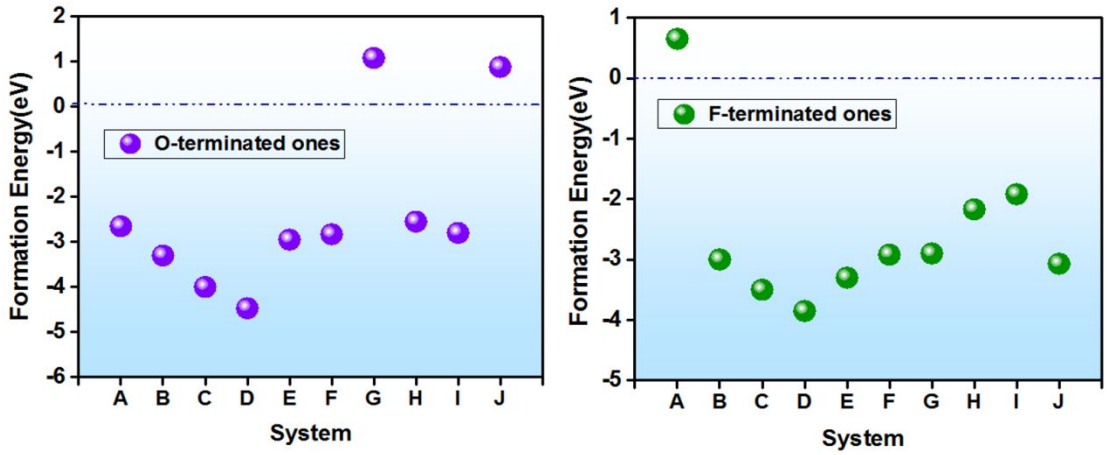

Figure S1 The formation energy of Pt single atom on M_2CT_2-V_T-Pt (T=O; F). A-J represent Sc_2CT_2-V_T-Pt, Ti_2CT_2-V_T-Pt, Zr_2CT_2-V_T-Pt, Hf_2CT_2-V_T-Pt, V_2CT_2-V_T-Pt, Nb_2CT_2-V_T-Pt, Ta_2CT_2-V_T-Pt, Cr_2CT_2-V_T-Pt, Mo_2CT_2-V_T-Pt, W_2CT_2-V_T-Pt, respectively.

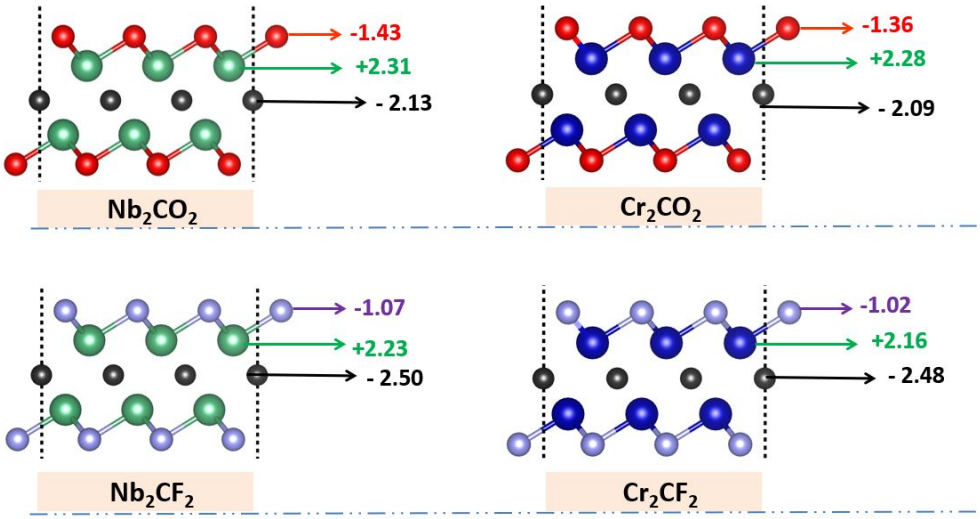

Figure S2 Bader charge populations of Nb_2CO_2, Cr_2CO_2 Nb_2CF_2 and Cr_2CF_2.

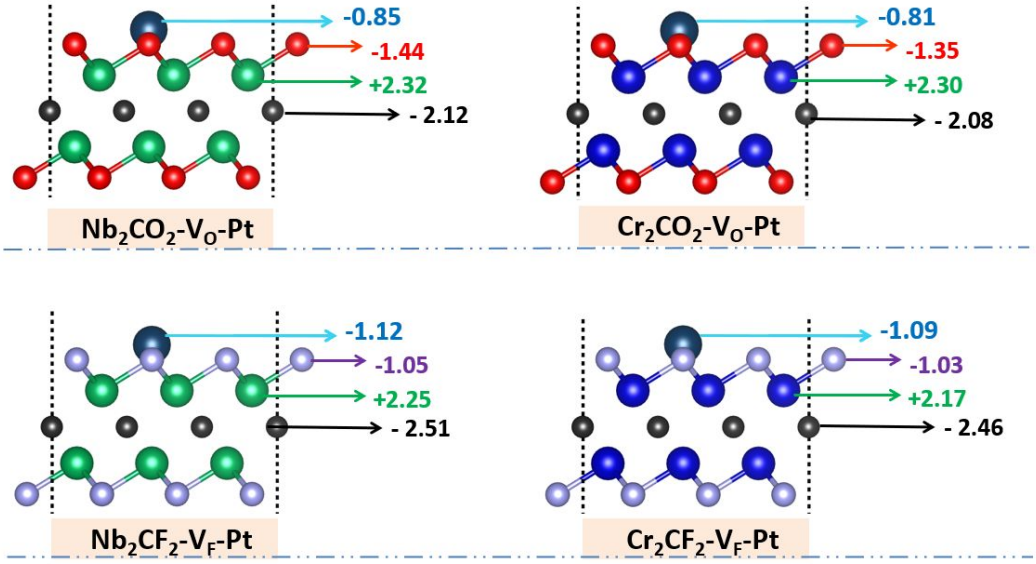

Figure S3 Bader charge populations of Nb_2CO_2-V_O-Pt, Cr_2CO_2-V_O-Pt, Nb_2CF_2-V_F-Pt and Cr_2CF_2-V_F-Pt.

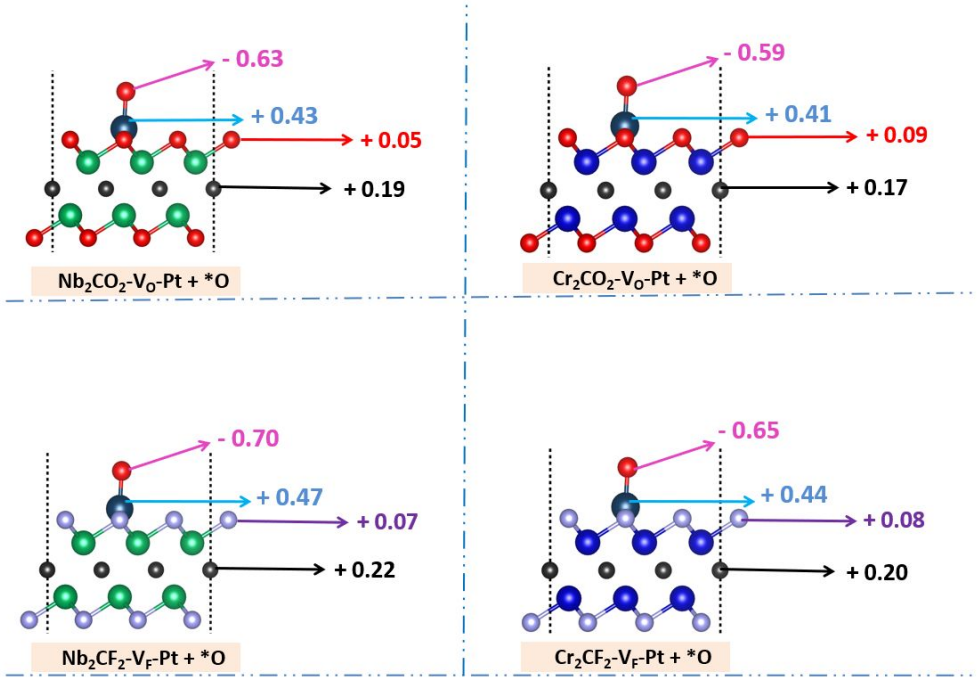

Figure S4 Bader charge populations of the O-atom adsorbed on Nb_2CO_2-V_O-Pt, Cr_2CO_2-V_O-Pt, Nb_2CF_2-V_F-Pt and Cr_2CF_2-V_F-Pt.

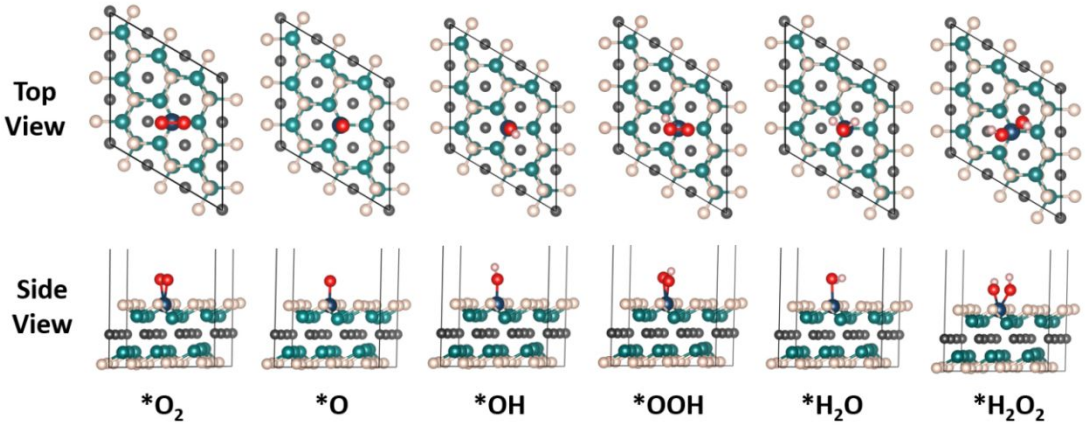

Figure S5 The geometric structures of O_2, O-atom, OH, OOH, H_2O and H_2O_2 adsorbed on the surface of Pt SACs.

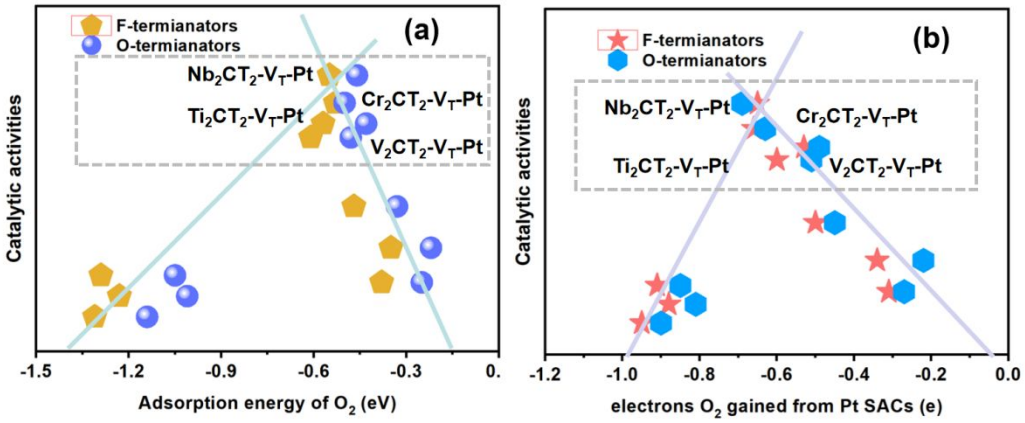

Figure S6 The relationship between catalytic activities and O_2 binding strength to Pt SACs, including (a) the adsorption energy of O_2 and (b) the electrons that O_2 gained.

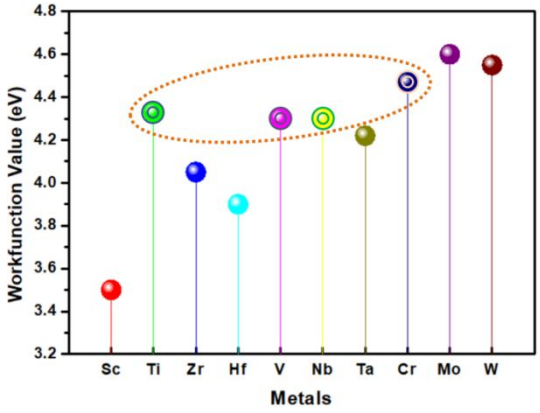

Figure S7 The work function values of the submetals in M_2CT_2-V_T-Pt (M= Sc, Ti, Zr, Hf, V, Nb, Ta, Cr, Mo, W; T=O, F).

(a)

(b)

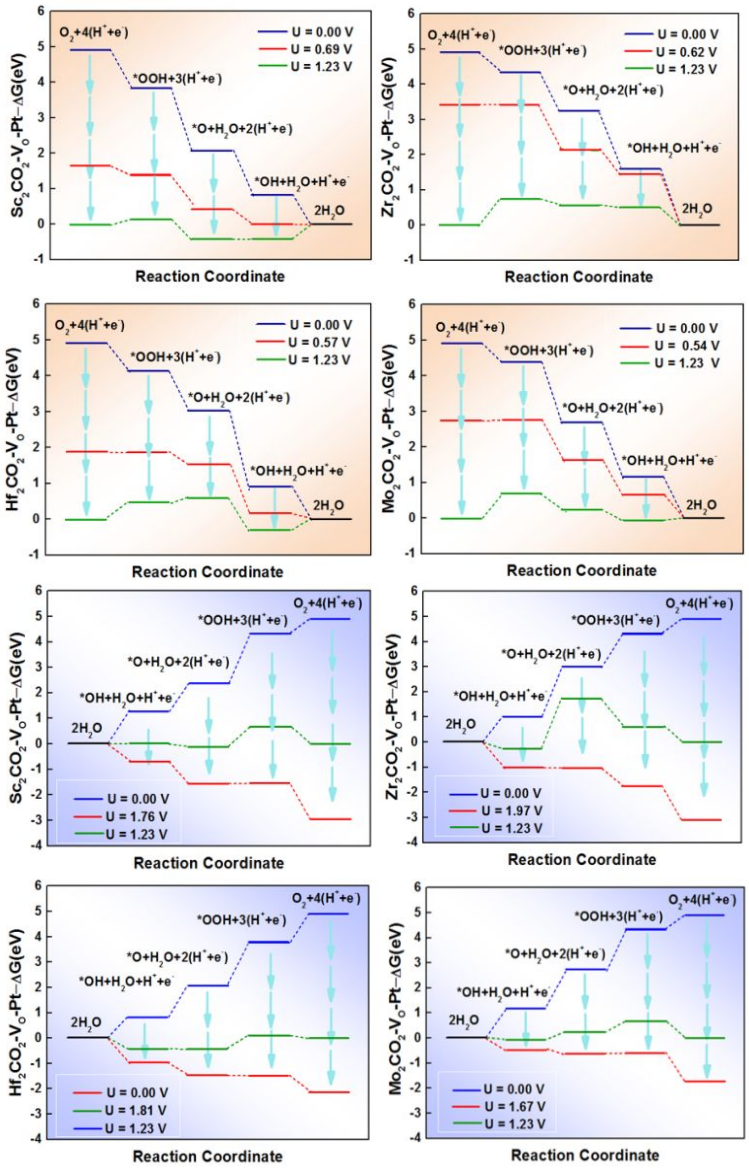

Figure S8 (a-b, respectively) The free energy diagram of the O-terminated Pt SACs (Hf_2CO_2-V_O-Pt, Zr_2CO_2-V_O-Pt, Mo_2CO_2-V_O-Pt) for the elementary ORR and OER steps, where the submetals are Zr, Hf, Ta, W and Mo, respectively.

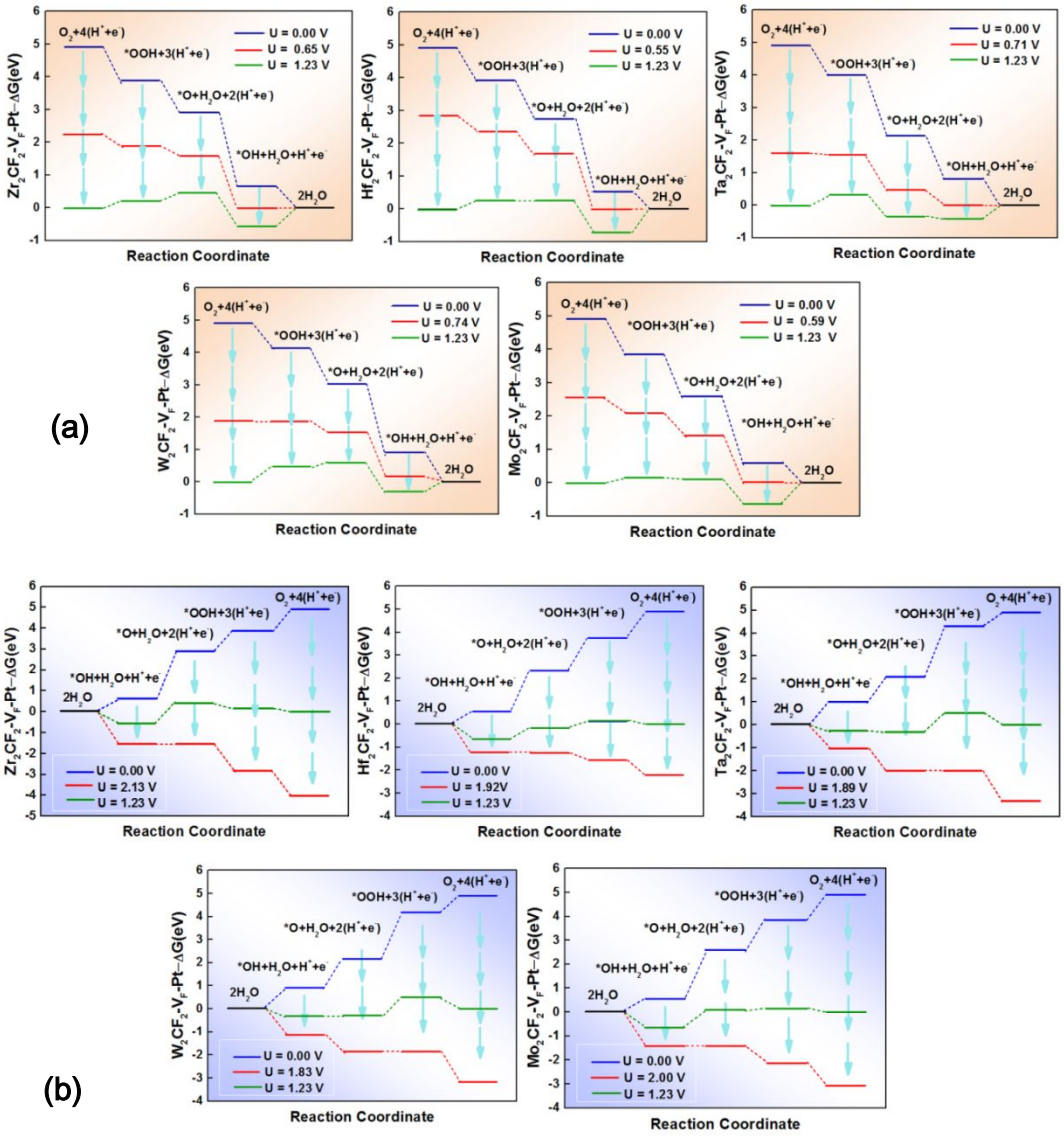

Figure S9 (a-b, respectively) The free energy diagram of F-terminated Pt SACs (Zr_2CF_2-V_F-Pt, Hf_2CF_2-V_F-Pt, Ta_2CF_2-V_F-Pt, W_2CF_2-V_F-Pt, Mo_2CF_2-V_F-Pt) for the elementary ORR and OER steps.

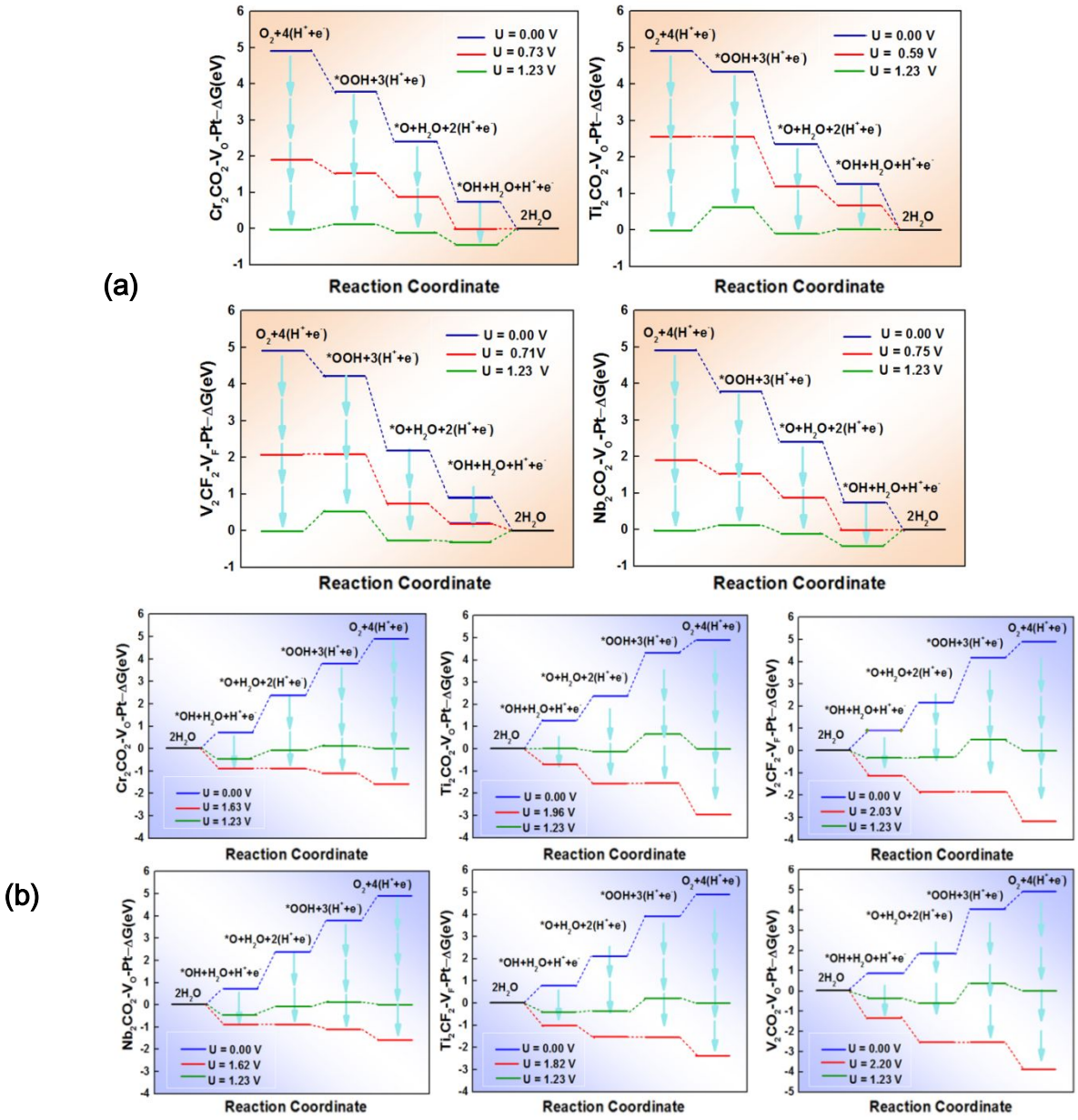

Figure S10 The free energy diagram of (a) Cr_2CO_2-V_O-Pt, Ti_2CO_2-V_O-Pt, V_2CF_2-V_F-Pt, Nb_2CO_2-V_O-Pt for the elementary ORR steps, and (b) Cr_2CO_2-V_O-Pt, Ti_2CO_2-V_O-Pt, V_2CF_2-V_F-Pt, Nb_2CO_2-V_O-Pt, Ti_2CF_2-V_F-Pt, V_2CO_2-V_O-Pt for the elementary OER steps.

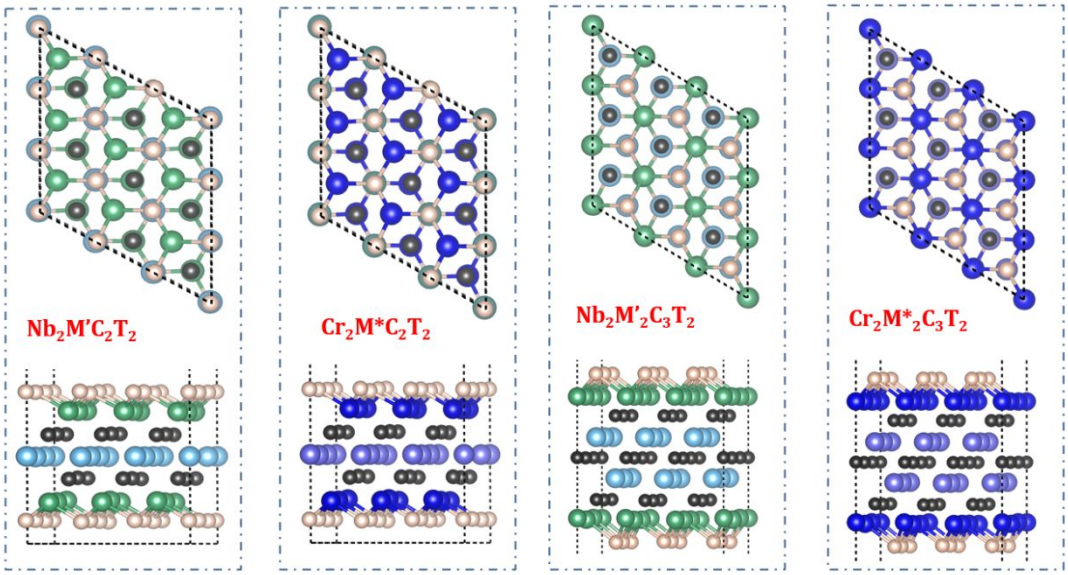

Figure S11 The geometric structures of the selected bimetal MXenes ($Cr_2M^*_2C_3T_2$, $Nb_2M'_2C_3T_2$, $NbM'C_2T_2$, $Cr_2M^*C_2T_2$).

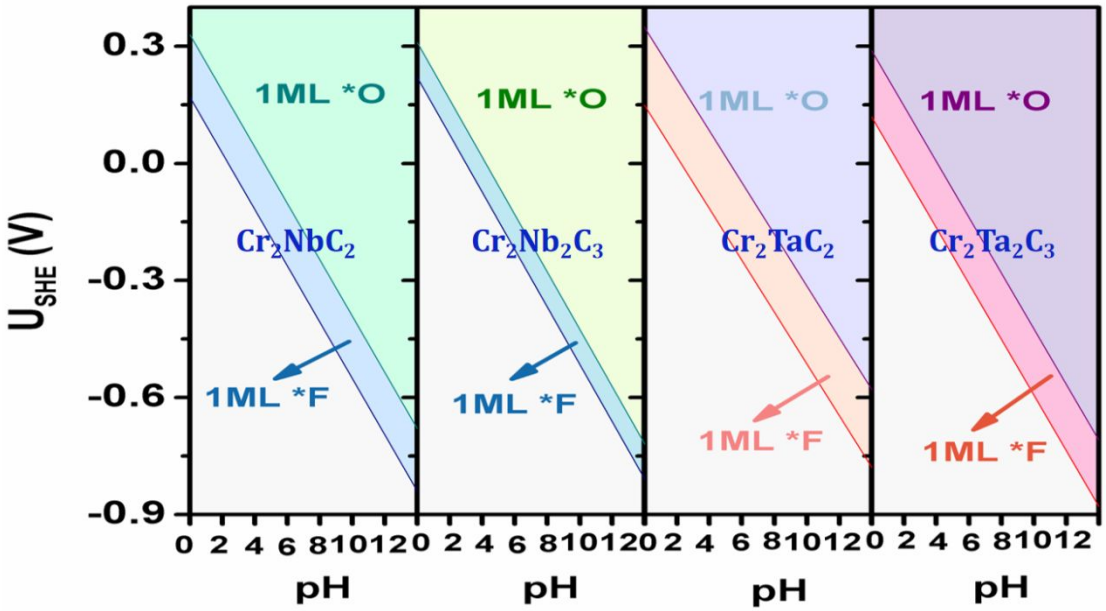

Figure S12 Surface Pourbaix diagrams of Cr_2NbC_2, $Cr_2Nb_2C_3$, Cr_2TaC_2 and $Cr_2Ta_2C_3$ with different functional groups.

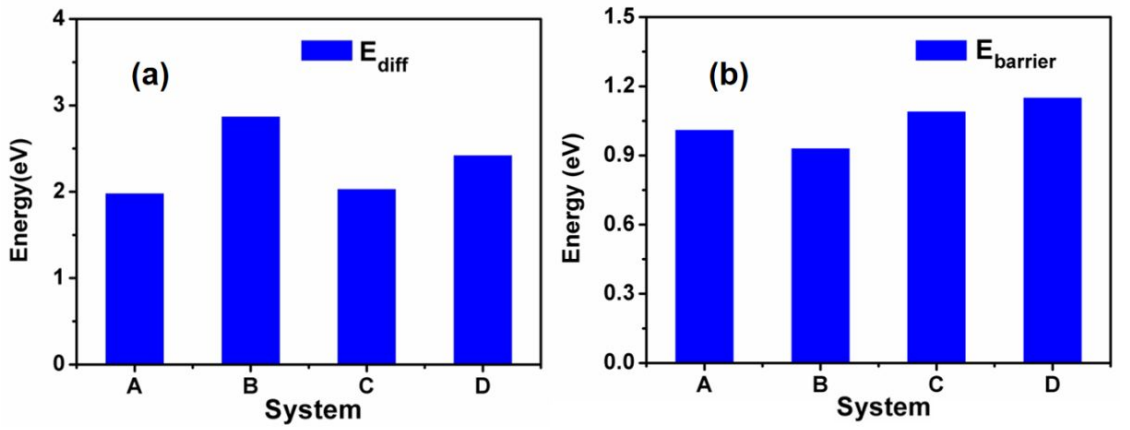

Figure S13 (a) The diffusion energy and (b) the energy barrier of Pt single atom on the Cr-based MXenes, A-D are $Cr_2NbC_2O_2$-V_O-Pt, $Cr_2Nb_2C_3O_2$-V_O-Pt, $Cr_2Ta_2C_3O_2$-V_O-Pt and $Cr_2TaC_2O_2$-V_O-Pt, respectively.

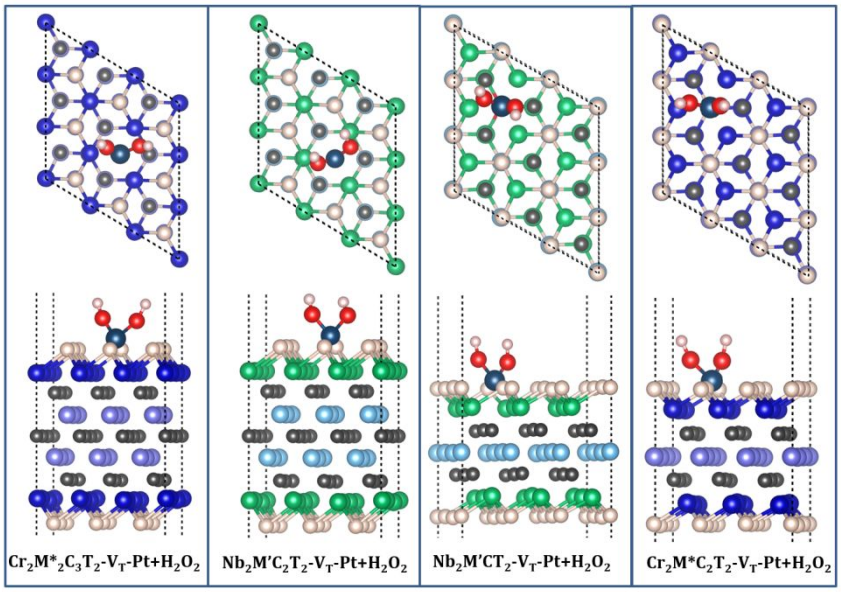

Figure S14 Geometric structures of H_2O_2 adsorbed on the surface of the bimetal Pt SACs ($Cr_2M^*_2C_3T_2$-V_T-Pt, $Nb_2M'_2C_3T_2$-V_T-Pt, $NbM'C_2T_2$-V_T-Pt, $Cr_2M^*C_2T_2$-V_T-Pt).

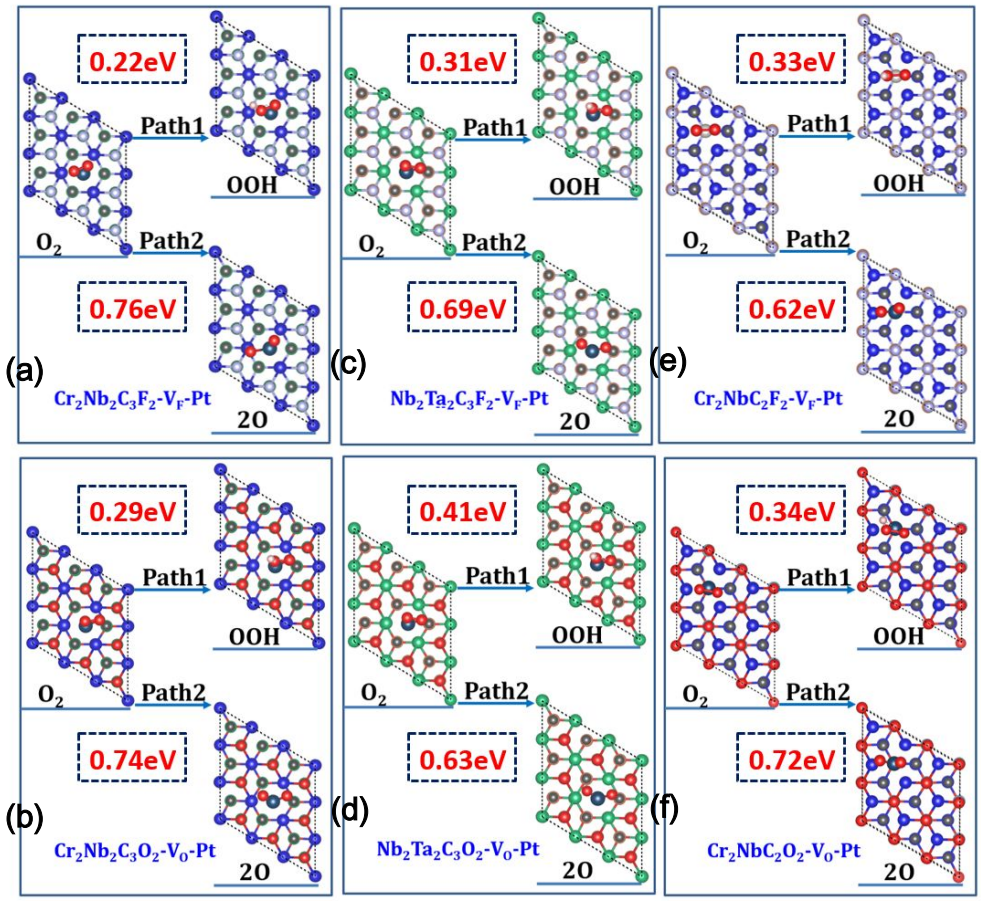

Figure S15 The reaction competition of O_2 hydrogenation (path 2) or dissociation (path 1) at the first step of ORR. a)-f) represent $Cr_2Nb_2C_3F_2$-V_F-Pt, $Cr_2Nb_2C_3O_2$-V_O-Pt, $Nb_2Ta_2C_3F_2$-V_F-Pt, $Nb_2Ta_2C_3O_2$-V_O-Pt, and $Cr_2NbC_2F_2$-V_F-Pt, $Cr_2NbC_2O_2$-V_O-Pt, respectively.

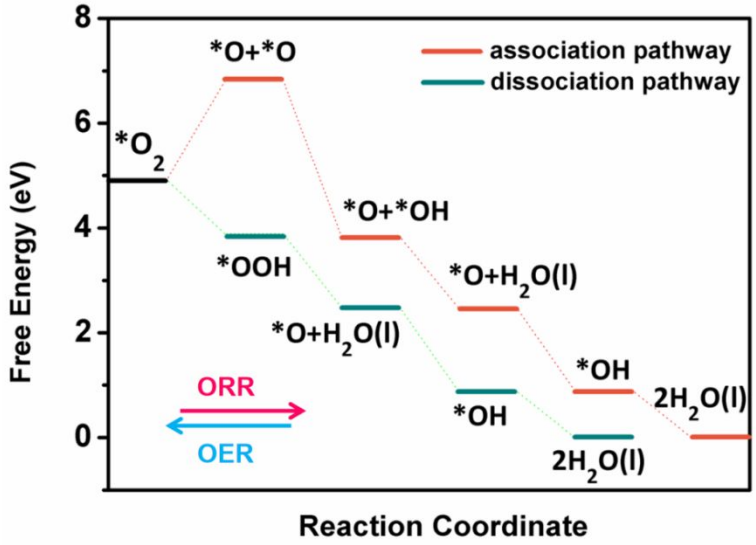

Figure S16 The thermodynamic processes of ORR on $Cr_2Nb_2C_3O_2$-V_O-Pt, including association and dissociation pathways.

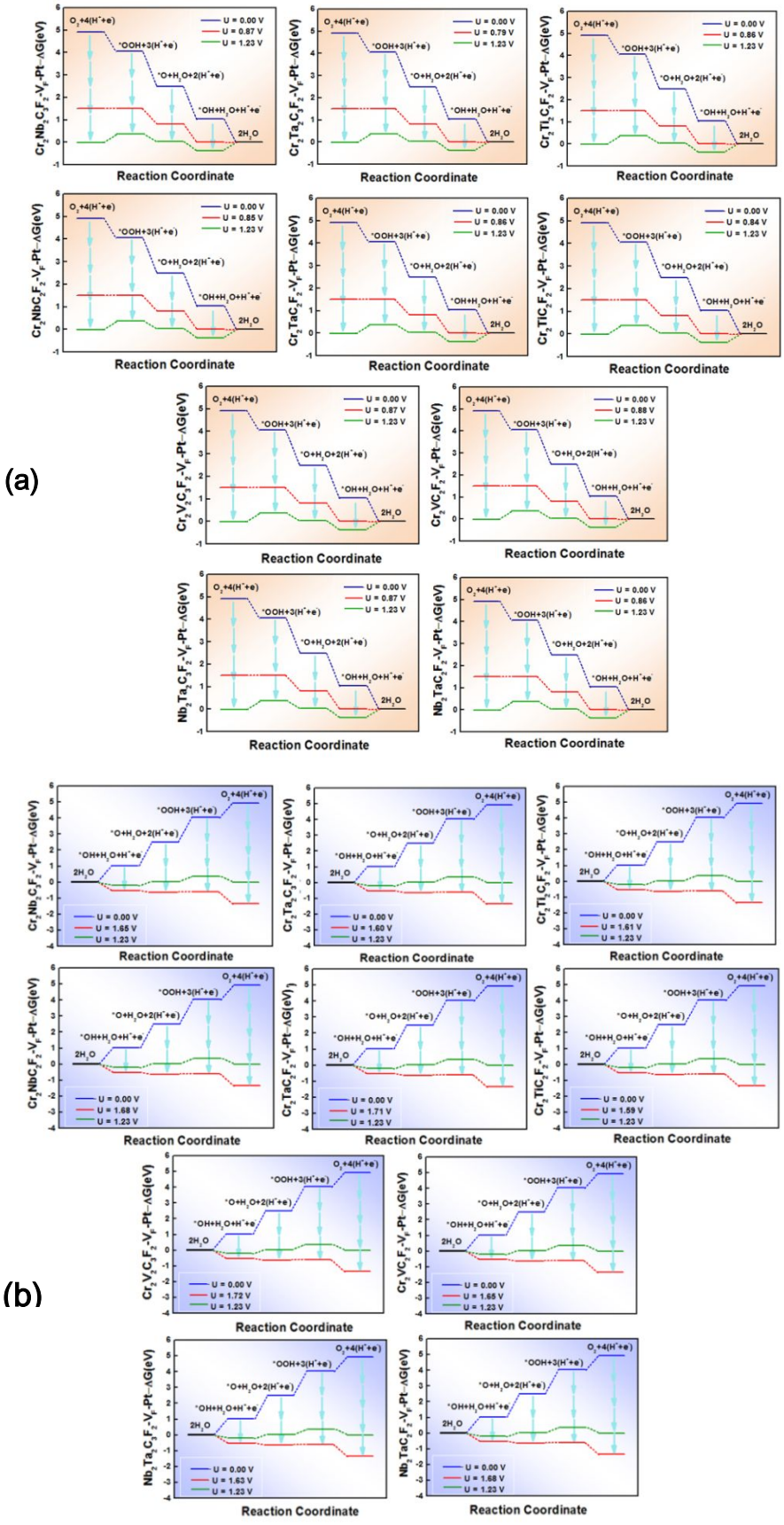

Figure S17 (a-b, respectively) The free energy diagram of the F-terminated bimetal Pt

SACs ($Cr_2Nb_2C_3F_2$-V_F-Pt, $Cr_2Ta_2C_3F_2$-V_F-Pt, $Cr_2Ti_2C_3F_2$-V_F-Pt, $Cr_2V_2C_3F_2$-V_F-Pt, $Cr_2NbC_2F_2$-V_F-Pt, $Cr_2TaC_2F_2$-V_F-Pt, $Cr_2TiC_2F_2$-V_F-Pt, $Cr_2VC_2F_2$-V_F-Pt, $Nb_2Ta_2C_3F_2$-V_F-Pt, $Nb_2TaC_2F_2$-V_F-Pt) for the elementary ORR and OER steps.

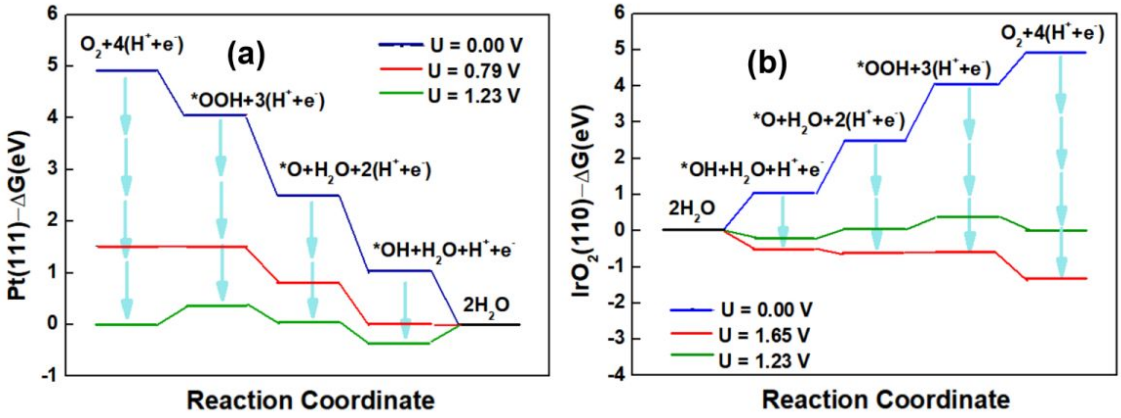

Figure S18 The free energy diagram of (a) ORR on Pt (111) and (b) OER on IrO_2(110).

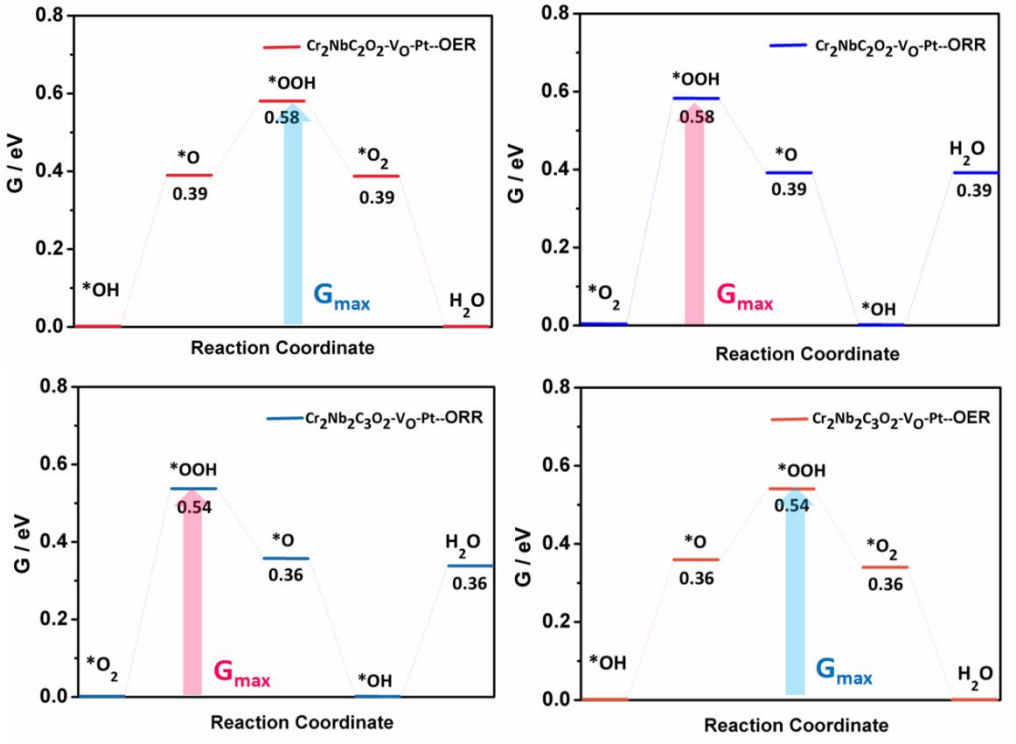

Figure S19 The mechanistic description (G_{max}) of ORR and OER on $Cr_2NbC_2O_2$-V_O-Pt and $Cr_2Nb_2C_3O_2$-V_O-Pt.

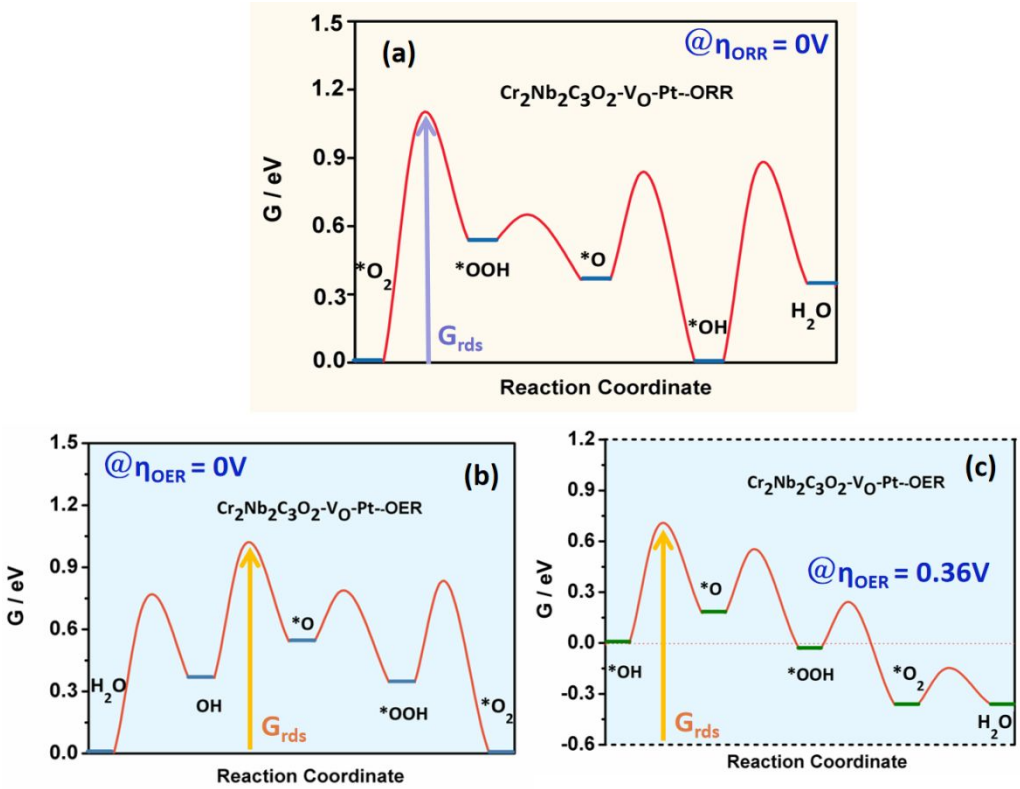

Figure S20 The rate-determining step and the relative free energy on $Cr_2Nb_2C_3O_2$-V_O-Pt for (a) ORR at overpotential of 0 V, (b) OER at overpotential of 0 V and (c) OER at overpotential of 0.36 V.

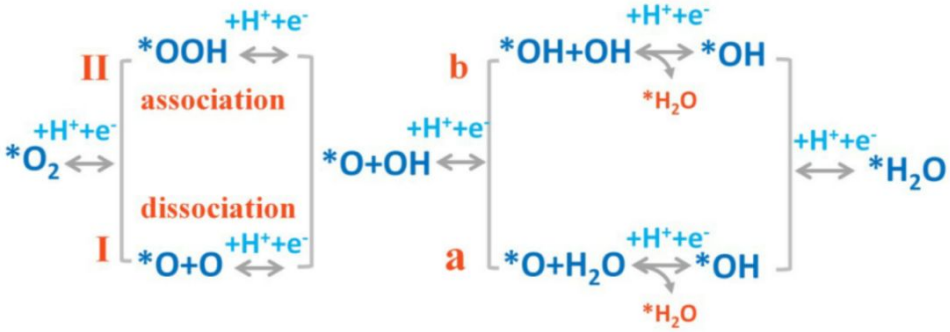

Figure S21 The two possible reaction pathways as well as the proton-electron transfer process in the association mechanism.

S-2 More calculation details

The overall ORR reaction in the acidic environment was written in Eq (1), like that occurs on the cathode of a fuel cell in discharge:

$$O_2 + 4H^+ + 4e^- \rightarrow 2H_2O \quad (1)$$

According to literatures, this ORR reaction proceeds via the 4-electron transfer pathways as shown in Eq 1a-1d:

$$*+ O_2\,(g) + e^- + H^+ \rightarrow *OOH \quad (1a)$$

$$*OOH + e^- + H^+ \rightarrow H_2O\,(l) + *O \quad (1b)$$

$$O* + e^- + H^+ \rightarrow *OH \quad (1c)$$

$$*OH + e^- + H^+ \rightarrow H_2O\,(l) + * \quad (1d)$$

In which * denotes an activity site on the catalyst, (l) and (g) represent liquid and gas phase, respectively.

The OER is the reverse reaction of ORR that described in Eq (2):

$$2H_2O \rightarrow O_2 + 4e^- + 4H^+ \quad (2)$$

with the 4-electron transfer pathways given in Eq 2a-2d:

$$H_2O\,(l) + * \rightarrow *OH + e^- + H^+ \quad (2d)$$

$$*OH \rightarrow O* + e^- + H^+ \quad (2b)$$

$$H_2O\,(l) + *O \rightarrow *OOH + e^- + H^+ \quad (2c)$$

$$*OOH \rightarrow *+ O^2\,(g) + e^- + H^+ \quad (2d)$$

S-3 The diffusion energy

To evaluate the clustering tendency of the adatoms, the cohesive energy of the corresponding bulk metal was considered. The diffusion energy (E_{diff}) were defined as

$$E_{diff} = E_{ads} - E_{coh} \quad (3)$$

where E_{ads} and E_{coh} denotes the adsorption energy and cohesive energy of the corresponding transition-metal bulk per metal atom, respectively, where were defined as follows:

$$E_{ads} = -[E_{Pt@MXenes} - (E_{MXenes} + E_{Pt}) \quad (4)$$

where $E_{Pt@MXenes}$ was the total energy of the MXene layer with Pt adatom attached, E_{MXenes} was the total energy of the bare MXene, and E_{Pt} was the energy of an isolated Pt atom,

$$E_{coh} = E_{at} - \frac{E_{bulk}}{N} \quad (5)$$

where E_{at} was the energy of the isolated metal atom in vacuum and E_{bulk} was the energy of the bulk unit cell containing N atoms.

S-4 The Pourbaix diagrams of O and F terminators

To further realize their stability in experiment and acidic ORR/OER environment, the

Pourbaix diagrams of O and F terminators on the selected Cr-based bi-metal MXenes were studied referring to previous literature[1-2]. The corresponding data are summarized in Figure S12, where the U_{SHE} of all O and F terminators are positive on these MXenes. However, the U_{SHE} values of O are more positive than those of F, which indicates the higher stability of O-terminated MXenes in experiment and acidic ORR/OER environment.

S-5 Association and dissociation pathways

To consider the H^+ and e^- species on the reaction path in a standard procedure, the depicts free-energy diagrams including association pathway and dissociation pathway at zero overpotential is supplemented (taken $Cr_2Nb_2C_3O_2$-V_O-Pt as example). As shown in Figure S16, the distinction of the free energy in the association path and the dissociation path is before the formation of *O. The potential determining step of ORR is $*O_2 + H^+ + e^- \rightarrow *OOH$ for the associative path and $*O_2 \rightarrow *O + *O$ for the dissociative path, with an overpotential of 0.36 V and 1.75 V, respectively. For the OER process, the potential determining step is $*OH + H_2O_{(l)} \rightarrow *O + H_2O_{(l)} + H^+ + e^-$ for the association path and $*O + *O^* \rightarrow O_2$ for the dissociative path, with an overpotential of 0.37 V and 3.12 V, respectively. Hence, from the thermodynamic aspect, the association mechanism is also more favorable than the dissociation mechanism for its smaller ORR and OER overpotentials.

S-6 The mechanistic description

To further confirm the activity trend, the free-energy changes among the mechanistic description (G_{max}) are taken into account. As shown in Figure S19, the G_{max} that the transition from *O adsorbate to *OOH are 0.54 eV and 0.58 eV on $Cr_2NbC_2O_2$-V_O-Pt and $Cr_2Nb_2C_3O_2$-V_O-Pt, respectively, both of which are much lower than that of ORR on Pt(111) and OER on IrO_2 (110) (0.75 eV and 0.92 eV, respectively). This again demonstrates the bi-functional catalysis activity of $Cr_2NbC_2O_2$-V_O-Pt and $Cr_2Nb_2C_3O_2$-V_O-Pt.

The rate-determining reaction step (RDS) of ORR and OER on $Cr_2Nb_2C_3O_2$-V_O-Pt were also studied to clarify the practical activity based on the full free-energy diagram. As shown in Figure S20, the RDS of ORR was formed when O_2 turned to *OOH at 0V overpotential. While both the RDS of OER was the step of *O formation at the overpotential of 0V or 0.36 V. This result is consistent with the discussion in the main text.

References

1. Zhan, C.; Sun, W.; Xie, Y.; Jiang, D.; Kent, P. R. C. Computational Discovery and Design of MXenes for Energy Applications: Status, Successes, and Opportunities. *ACS Appl. Mater. Interfaces*, **2019**, 11, 24885−24905

2. Gao, G.; O'Mullane, A. P.; Du, A. 2D MXenes: A New Family of Promising Catalysts for the Hydrogen Evolution Reaction. *ACS Catal.* **2017**, 7, 494−500